Available online at www.sciencedirect.com
ScienceDirect
Trans. Nonferrous Met. Soc. China 30(2020) 1535−1549
Transactions of Nonferrous Metals Society of China
www.tnmsc.cn

Nanodiamond incorporated sol−gel coating for corrosion protection of magnesium alloy

S. NEZAMDOUST, D. SEIFZADEH, A. HABIBI-YANGJEH

Applied Chemistry Department, Faculty of Science, University of Mohaghegh Ardabili, Ardabili, Iran

Received 30 July 2019; accepted 30 April 2020

Abstract: Sol−gel coatings containing various amounts of hydroxylated nanodiamond (HND) particles were applied on the magnesium alloy for corrosion protection. The micrometric defects in the sol−gel coating completely disappeared after adding 0.01, 0.02 and 0.05 wt.% of the HND nanoparticles. The AFM analyses showed that average roughness of the sol−gel film is about 6.7 nm which increases to 16.1 and 20.2 nm after incorporating 0.005 and 0.02 wt.% of the HNDs, respectively. The corrosion resistance of the coatings was tested in Harrison's solution by means of EIS technique after 15, 30, 60 and 120 min immersion. The corrosion resistance of the sol−gel coating was remarkably enhanced by incorporating different contents of the HNDs and the best result was obtained for 0.01 wt.%. The results of the EIS experiments were confirmed by the potentiodynamic polarization tests. The corrosion resistance enhancement was attributed to the film compactness (due to the chemical interaction with the HNDs), formation of tortuous pathways for diffusion of the corrosive solution, and filling of the defects by the nanoparticles. However, the beneficial effect of the HNDs on the corrosion resistance gradually diminished as the content of nanoparticle was increased. Finally, the micromorphology of the sol−gel nanocomposites was studied after the corrosion tests.
Key words: magnesium alloy; corrosion; coating; sol−gel; nanodiamond

1 Introduction

Magnesium alloys with a density of about 1.7−2 g/cm^3 are lighter than other structural metals and therefore are being increasingly used in transportation and aerospace industries [1−3]. However, magnesium alloys have high electro-chemical reactivity and hence poor corrosion resistance. In addition, these alloys are prone to the galvanic corrosion which occurs between the magnesium matrix and second phases or impurities (micro-galvanic corrosion) in the alloy or in contact with other structural metals [4,5]. Therefore, it is necessary to improve the resistance of the magnesium alloys against the corrosion before using of them in outdoor applications. Conversion film, organic coating, micro arc oxidation (MAO), layered double hydroxide (LDH), etc, are the most cost-effective and useful strategies for corrosion protection of the magnesium-based substrates [6−13].

Another surface technology is the sol−gel coating which has recently attracted much attention as a simple and environmentally-friendly method. The sol−gel process has a number of advantageous properties such as mild pressure and temperature, high homogeneity, possibility of the coating application on the substrates with complex shape, and chemical/thermal stability of the resultant film [14−17]. Also, the sol−gel films show good adhesive strength due to the formation of covalent links with the metal surface. However, the sol−gel coatings typically contain many structural defects (such as cracks, pores, and parts with low cross-linking density) that allow the corrosive agents to

Corresponding author: D. SEIFZADEH; Tel: +98-4533514702; Fax: +98-4533514701; E-mail: seifzadeh@uma.ac.ir, dseyfzadeh@yahoo.com
DOI: 10.1016/S1003-6326(20)65317-1

penetrate toward the film/metal interface. Cracks and pores in sol−gel coatings generally form during the heat treatment process due to the rapid evaporation of unreacted water and alcohols. Besides, difference between expansion thermal coefficients of the substrate and sol−gel film is another main reason of the defect formation during the curing process.

Hybrid organic−inorganic sol−gel films can be obtained by adding the organo-modified components to the inorganic ceramic network. Compared to the inorganic sol−gel films, the hybrid sol−gel films are flexible, thick, and defect-free and can be obtained at lower curing temperatures. The hybrid sol−gel films have been frequently used to increase the corrosion resistance of different substrates [18,19]. Also, addition of the nano-structures causes the enhancement in the barrier properties of the sol−gel coating due to the filling of the possible defects and the formation of more compact ceramic structure. For instance, it has been indicated that the anticorrosion and mechanical properties of the sol−gel film can be enhanced by addition of SiO_2 nanoparticles [20]. PERES et al [21] have also prepared silica-loaded hybrid sol−gel nanocomposites on AZ31 Mg alloy by using tetraethoxysilane (TEOS) and 3-glycidoxypropyl trimethoxysilane (GPTMS) precursors. Based on the electrochemical impedance spectroscopy (EIS) analyses, the coating with 300 mg/L SiO_2 nanoparticles showed the greatest value of the corrosion resistance. Additionally, CLAIRE et al [22] have synthesized a multilayer alumino-silicated epoxy-based sol−gel coating on stainless steel containing zirconia nanoparticles and the applied nanocomposites showed good corrosion and wear resistance. Also, silane sol−gel films containing various concentrations of sodium montmorillonite nanoclays were deposited on the galvanized steel substrate [23]. It was revealed that the barrier characteristics of the sol−gel film are remarkably promoted by incorporation of 2 wt.% nanoclay. ASADI et al [24] have prepared nanocomposite sol−gel coatings with various contents of cloisite nanoparticles for deposition on the steel substrate. The nanocomposite with 0.1 wt.% cloisite showed the best protection performance so that its corrosion resistance was two magnitude orders greater than the neat silane film after 4 h immersion in the NaCl corrosive media due to the formation of a dense silica film and good dispersion of the nanoparticles in the silica network. Also, the influence of curing conditions (time and temperature) on the corrosion protection of the hybrid silane layer loaded with the clay nanoparticles was investigated by FEDEL et al [25]. They reported that the high curing temperature causes the formation of a dense film on galvanized steel which sufficiently reduces the cathodic current and so, leads to the enhancement of corrosion resistance. Also, it was found that the formation of an intermediate layer between the sol-gel nanocomposite and steel substrate is responsible for better anticorrosion performance. Also, YU et al [26] has prepared CuO/SiO_2 and NiO/SiO_2 nanocomposite films on aluminum alloy by in-situ synthesis of CuO and NiO nanoparticles in the sol solution. The corrosion protection and thermal conductivity of the coatings were improved after the addition of the nanoparticles.

In recent years, carbon nanostructures (graphene, fullerenes, nanodiamond and carbon nanotubes) are extensively used as nano-filler in the composite materials due to their appropriate properties such as excellent functionalization ability, high aspect ratio, high mechanical strength, good electrical properties, and excellent chemical inertness [27,28]. There are few report about incorporation of carbon nanostructures in the sol-gel coatings as promoter of the corrosion resistance. For example, LI et al [29] added functionalized graphene oxide (GO) nanosheets as reinforcement to a hybrid silane coating in order to enhance the corrosion protection properties. The surface of the GO was functionalized by TEOS molecules before addition to the sol in order to improve chemical interaction between the GOs and silane matrix. Also, RAMEZANZADEH et al [30] used a sol−gel based silane film (TEOS + 3-aminopropyl triethoxysilane) filled with silanized GO nanosheets as primer of epoxy coating on the steel substrate. Adding of GO nanosheets improved the anticorrosion performance of both sol−gel and epoxy coatings and decreased the cathodic delamination of composite coating. Furthermore, multi-walled carbon nanotubes (MWCNTs) were added to bis-[triethoxysilylpropyl] tetrasulfide (BTESPT) silane film by LIU et al [31]. The MWCNTs were carboxylated before incorporation in the sol−gel coating in order to get better chemical

interaction with the silane network. Electrochemical tests showed lower corrosion rate for the nanocomposite compared to the pure sol−gel film.

Nanodiamond (ND) has attracted much attention for application as nano-filler in the coatings due to its special properties, including mechanical stability, hardness, crystallinity, narrow particle size distribution, chemical inertness of core, and surface reactivity [32−34]. The effect of nanodiamonds inclusion on the anticorrosion performance of the sol−gel coatings has not been investigated yet, whereas they have several advantages such as relatively low-cost and commercial accessibility.

The aim of the present work is providing sufficient corrosion protection for the AM60B magnesium alloy by applying hybrid sol−gel coatings loaded with nanodiamond particles. First of all, the NDs were functionalized to increase the number of hydroxyl groups on the surface in order to obtain better dispersion and chemical interaction with the silane matrix. Afterward, the hybrid sol−gel film (TEOS+GPTMS) containing various contents of hydroxylated nanodiamonds (HNDs) was synthesized and then deposited on the magnesium alloy. Functionalized nanodiamond particles and sol−gel nanocomposites were characterized using several surface analysis techniques involving scanning electron microscopy (SEM), XRD (X-ray diffraction), FTIR (Fourier transform infrared), and AFM (atomic force microscopy). In addition, the effect of the nanodiamond addition on the corrosion protection capacity of the silane sol−gel coating was evaluated by the electrochemical corrosion tests and subsequent morphological analyses.

2 Experimental

2.1 Hydroxylation of ND particles

Nanodiamond particles (>98%) synthesized by detonation technique were supplied by US Research Nano (USRN). Before hydroxylation, a suspension containing 500 mg nanodiamond and 30 mL dry tetrahydrofuran (THF) was prepared and then was stirred for about 5 min. It should be mentioned that the THF was predried overnight by potassium hydroxide before using. Then, 5 mL of 1 mol/L BH_3.THF (AcroSeal) solution, as reducing agent, was gradually added while the solution was stirred. The suspension was refluxed for about 24 h and then slowly cooled down to environment temperature. Afterward, 2 mol/L HCl was added to the mixture until hydrogen evolution finished. The HND product was collected by centrifugation and then washed with distilled water and acetone until the pH of supernatant solution became 7. Finally, light gray product was dried at 60 °C for about 24 h in a digital oven [35].

2.2 Nanocomposite sol preparation

The hybrid sol was prepared by mixing 0.02 mol TEOS and 0.02 mol GPTMS precursors. Then, hydroxylated ND particles were dispersed in the solution for 20 min in ultrasound bath (BANDELIN SONOREX). In order to initiate the hydrolysis, acidic water (pH=1, HCl) was added to the sol with 1:1 alkoxy to H_2O molar ratio. The prepared sol was stirred by a magnetic stirrer (700 r/min) for 2 h at ambient temperature (≈23 °C) and finally, absolute ethanol with equivalent volume was added to decrease the viscosity. Nanocomposite coatings were prepared by adding various concentrations (0, 0.005, 0.01, 0.02 and 0.05 wt.%) of the hydroxylated nanodiamonds to the sol solution.

2.3 Deposition of coatings

The substrate used in this work was AM60B magnesium alloy plate (Nanjing Welbow Metals Company) having an elemental composition of 6.33 wt.% Al, 0.68 wt.% Zn, 0.24 wt.% Mn and balanced Mg. The alloy samples with a thickness of 2 mm were cut to a size of 3 cm × 1.5 cm and then polished with SiC sand papers of different grade numbers (100, 400, 800, and 1000). Next, the alloy pieces were cleaned with deionized water and then were dried by a warm air stream. Afterward, the samples were ultrasonically degreased in acetone (Atlas Shimi, 99 %) for about 20 min at 40 °C using the ultrasonic bath.

The silane coatings were applied on the samples using a dip coater device (Pasargad Nano Equipment). The withdrawn speed of the samples and immersing time in the sol solution was about 10 cm/min and 2 min, respectively. After deposition, the coated samples were exposed to thermal treatment in order to complete the condensation process and also to remove the residual water and alcohol. In order to avoid cracking, the coated

samples were initially held at 60 °C in a digital oven (Pars Azma Co.) for 2 h and then the temperature was increased to 130 °C with a slow speed of 2 °C/min. After 1 h curing, the coated samples were cooled to the environment temperature naturally.

2.4 Characterization

Scanning electron microscopy (LEO, VP 1430) was used to conduct morphological analysis of the ND and HND nanoparticles. Also the surface and cross-section morphologies of the prepared nano-composites were studied by the SEM. For the SEM analyses, an accelerating voltage of 15 kV and a backscattered electron detector were utilized under high vacuum condition and the samples were gold plated for 5 min under Ar gas flow (2 Pa) before the characterization. A Polaron sputter coater device with 1200 V direct voltage was used for the gold plating. Also, the silica coated specimens were carefully cut and then were mildly polished by fine (1000 and 2000 grits) SiC sandpapers for preparation of the cross-sectional area. Next, the cross-sectional areas of the coated samples were morphologically analyzed by the SEM after cleaning (with deionized water and ethanol) and gold plating in the above-mentioned manner. Topography and average surface roughness (R_a) of the sol−gel films were analyzed by the AFM device (Veeco CP-II) with boron-doped silicon cantilever operating in the contact mode and scanning scale of 5 μm × 5 μm. The FTIR spectra of the NDs and HNDs were recorded by Perkinelmer spectrum RX device. Also, the XRD patterns of the NDs and HNDs were obtained using a Philips Xpert analytical diffractometer by a Cu K_α source with wavelength of 0.154 nm.

2.5 Corrosion tests

Corrosion resistance of the nanocomposites was estimated by means of the electrochemical impedance spectroscopy (EIS) experiments in Harrison's solution (0.35 wt.% $(NH_4)_2SO_4$ and 0.05 wt.% NaCl). The tests were carried out at room temperature using a μautolab3 Potentiostat−Galvanostat connected to a personal computer with Nova 1.6 software. A typical electrochemical cell configuration, with a saturated Ag−AgCl electrode as reference electrode and a platinum sheet as auxiliary electrode, was used. The sol−gel coated samples, which were isolated by the epoxy resin to leave an exposed surface area of 1 cm^2, were used as the working electrode. The EIS examinations were performed in frequencies across the range from100 kHz to 0.01 Hz by applying 10 mV sine wave alternative voltage around φ_{corr} (corrosion potential). Prior to the EIS experiments, the samples were left in contact with 200 mL of the Harrison's corrosive electrolyte for different time.

In addition, the potentiodynamic polarization curves of the coated samples were recorded in the Harrison's solution after 3 h immersion by scanning the potential of the working electrode with a rate of 1 mV/s from the cathodic to anodic direction using the above-mentioned electro-chemical cell arrangement.

3 Results and discussion

3.1 Characterization of nanoparticles

Surface of the detonation ND particles contains many functional groups such as carboxyl, lactone, hydroxyl and ketone. Hydroxyl groups on the ND particles can be chemically attached to the silanol groups of the hydrolysed silane precursors via condensation reaction. On the other hand, the strong chemical interaction between the silane matrix and incorporated ND particles may improve the nanoparticles dispersion in the sol−gel film. This is important from the corrosion protection point of view since agglomeration of the incorporated nanoparticles causes the formation of defects and discontinuities in the coatings as potential penetration pathways for the corrosive species. Also, good conjugation enhances the reinforcement effect of the nanoparticles in the matrix. It is obvious that the increase in the number of hydroxyl group on the nanodiamond can provide new possibilities for better chemical interaction with the silane network. Borane is able to reduce the carbonyl functional groups on the NDs, leading to the formation of homogeneous hydroxylated surface. Therefore, the nanodiamond particles were hydroxylated using borane reducing agent according to the experimental procedure that was previously explained elsewhere [35−37]. Generally, it is difficult to confirm the enrichment of the hydroxyl groups on the ND particles after reduction process due to the adsorption of water by both the raw and hydroxylated ND particles. However, the

FTIR spectra of the ND and HND particles are recorded (Fig. 1). Complete agreement between the recorded FTIR spectra with those obtained previously [35,37] was observed, indicating successful hydroxylation of the ND particles. The C—H stretching bands at around 2800−3000 cm^{-1} with a considerable intensity can be observed before and after the hydroxylation. Also, a wide adsorption band at around 3100−3600 cm^{-1} associated with O—H stretching modes of the adsorbed water can be easily detected. Furthermore, a number of new IR bands at 800−1000 cm^{-1} which are characteristics of the hydroxylated nanodiamonds are observed in FTIR spectrum of HND. The peak at 1258 cm^{-1} can be assigned to δ-OH vibration and bands at around 1000−1200 cm^{-1} may be ascribed to C—O vibration of alcohol groups [38].

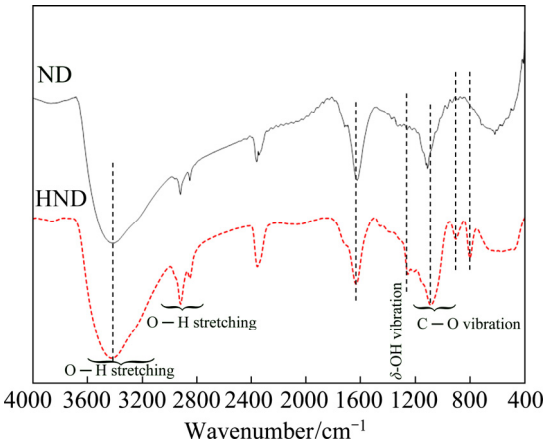

Fig. 1 FTIR spectra of ND and HND particles

Also, the XRD patterns of the nanodiamond particles before and after the hydroxylation are shown in Fig. 2. There is no significant difference in the XRD patterns of the ND and HND particles. This result is due to the fact that the hydroxylation process only modifies the surface chemistry of the particles and the crystalline structure stays unchanged [38]. However, the broad peak at 2θ=20°−30° corresponding to the graphitic fragments on the surface of the nanoparticles disappeared since the raw nanodiamonds were practically purified by the hydroxylation [39].

Moreover, the morphological features of the ND and HND particles were compared to each other by using the SEM technique. Figures 3(a) and 3(b) display the morphological images of the ND and HND particles, respectively. No significant

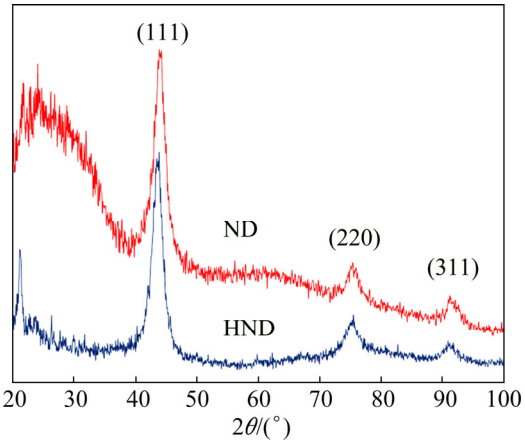

Fig. 2 XRD patterns of ND and HND particles

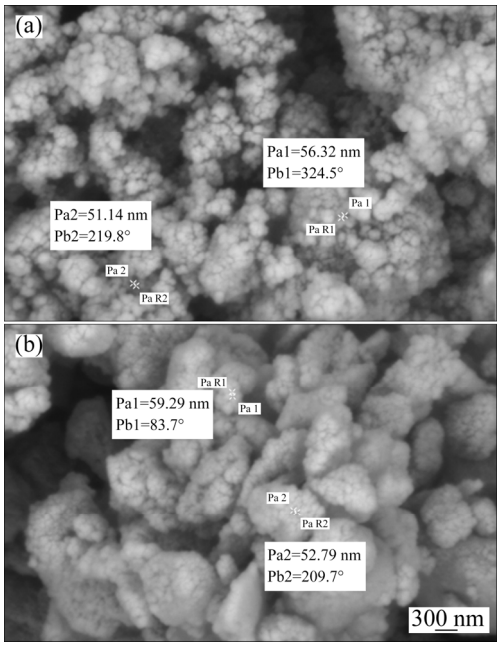

Fig. 3 SEM images of ND (a) and HND (b) particles

morphological difference was observed between the raw and hydroxylated nanodiamond particles. Also, it is clear that the ND and HND particles tend to form agglomerates owing to the high surface energy and the presence of active groups.

3.2 Characterization of coatings

SEM morphological images of the sol−gel films containing 0, 0.005, 0.01, 0.02 and 0.05 wt.% of the HND particles are represented in Fig. 4.

Relatively uniform and continuous sol−gel coating (Fig. 4(a)) can be seen on the magnesium alloy. However, some micro-sized defects can be easily detected on the pure sol−gel film. The existence of such defects is related to the reaction

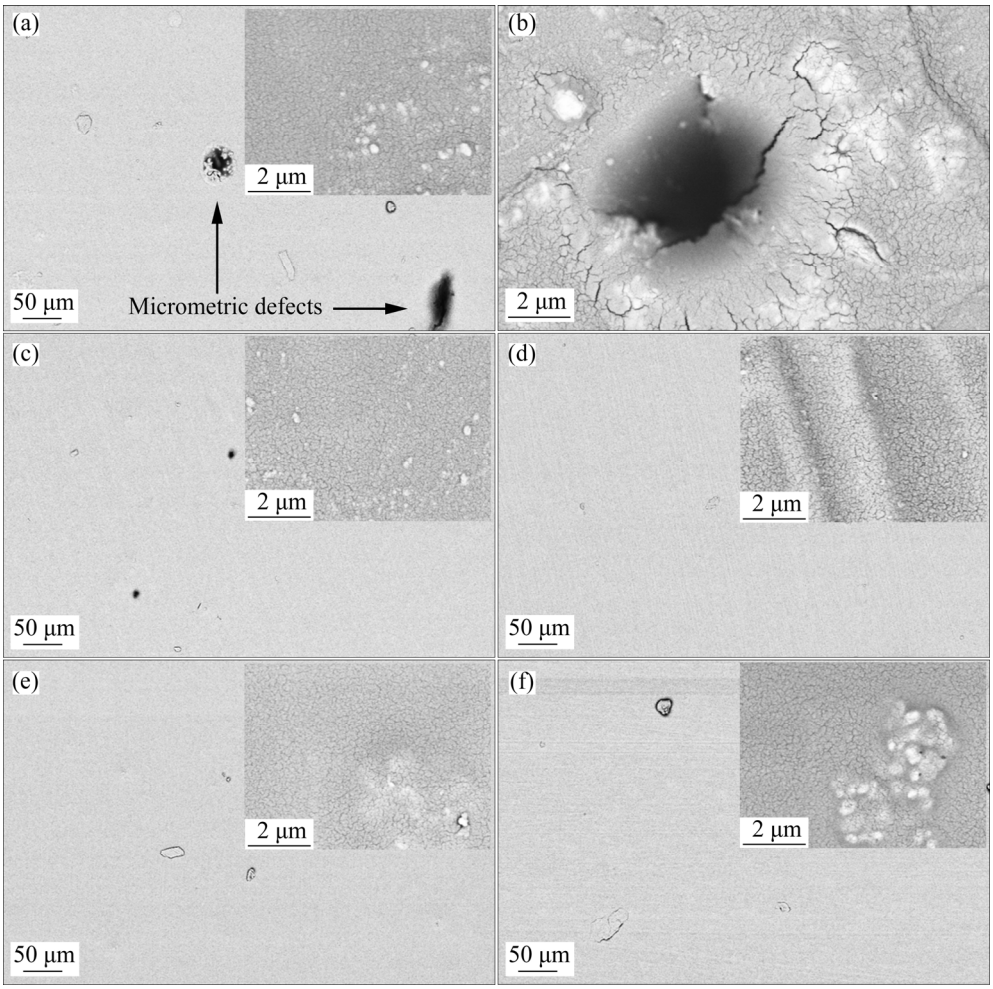

Fig. 4 SEM images of silane nanocomposites containing 0 (a, b), 0.005 (c), 0.01 (d), 0.02 (e) and 0.05 wt.% (f) of HND particles

between the active magnesium alloy and acidic sol solution, which leads to the formation of hydrogen gas bubbles and hence, the pores and other local defects in the final silica film. One of the observed micrometric defects is illustrated at high magnification in Fig. 4(b). Such defects have been previously seen in the monolayer sol−gel films on the magnesium alloys and may be removed by applying multilayer sol−gel films [7]. Also, some nanometric cracks can be seen in the high-magnification SEM image inserted in Fig. 4(a). Such nanometric defects in the sol−gel coatings form during evaporation of the solvents in the curing process [40]. After incorporation of the HND nanoparticles at concentration of 0.005 wt.%, the size and number of the micrometric defects were significantly decreased. Also, the micrometric defects were completely removed after loading of the HND particles at higher concentrations (0.01, 0.02 and 0.05 wt.%). These observations are more probably related to the existence of strong chemical interaction between the embedded particles and sol−gel coating via their hydroxyl groups as mentioned above. The mechanism of the chemical interaction has been schematically illustrated in Fig. 5.

As it is clear, the HND particles have more possibilities for chemical interaction via condensation reaction with the sol−gel matrix compared to the raw ND particles. Based on the illustrated scheme, each HND particle acts as bridge between several hydrolyzed silane precursors to form defect-free and compact sol−gel film on the magnesium alloy. In the other words, it seems that the HND addition causes the promotion of the chemical interaction between the silane monomers leading to the formation of more compact sol−gel coating. However, there is no

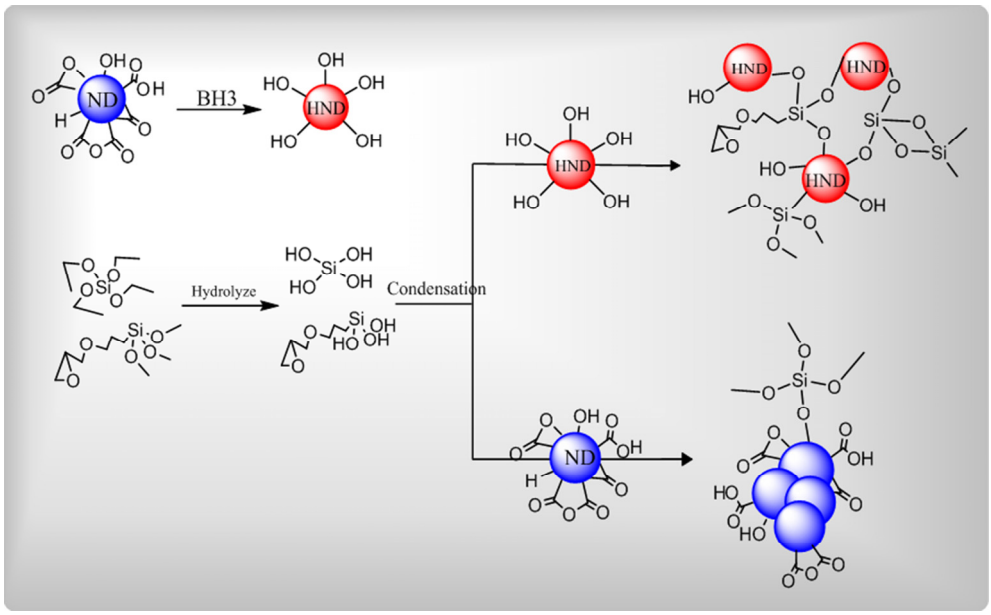

Fig. 5 Schematic illustration of chemical interaction between HND particles and sol−gel coating

significant morphological difference between the high-magnification SEM images before and after incorporation of the HND particles at different concentrations so that the nanometric defects were observed in all of the applied coatings.

In addition, agglomeration tendency of the incorporated HND particles is minimized due to their strong chemical interaction with the silane network so that no agglomeration was observed in the SEM images of the nanocomposites containing 0.005, 0.01 and 0.02 wt.% of the HND. However, partial agglomeration was observed in the sample with the highest concentration of the HND (0.05 wt.%).

The thickness of the sol−gel coating is a very important parameter which influences its corrosion protection properties. Thus, the thickness of the sol−gel coatings was evaluated by the cross-sectional SEM images before and after incorporation of the HND particles (at 0.01 wt.% concentration). The thickness of the hybrid coatings either before (Fig. 6(a)) or after (Fig. 6(b)) incorporation of the HND particles was about 0.7−0.8 μm, meaning that the nanoparticles addition did not change the film thickness. Similar results were observed for other concentrations of the HND but the results were not reported here to avoid the repetition. Additionally, the film detachment was not seen at the substrate/coating interface more probably due to the formation of covalent bond

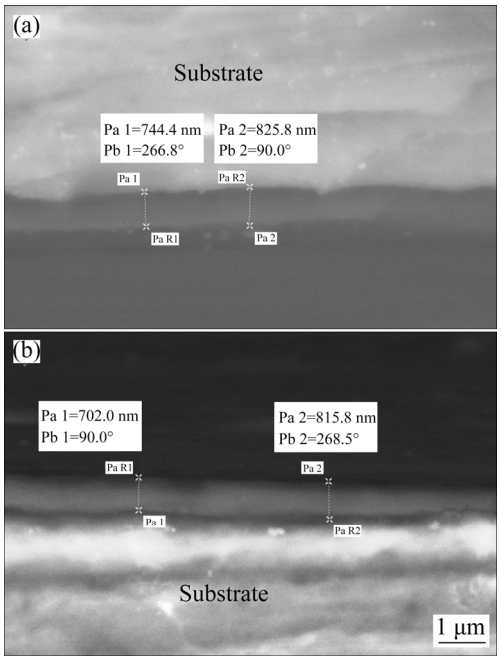

Fig. 6 Cross-sectional views of sol−gel coating containing 0 (a) and 0.01 wt.% (b) of HND particles

(Mg — O — Si) between the silane coating and magnesium alloy surface [40].

The effect of the HNDs incorporation on the surface roughness of the sol−gel film was also investigated by the AFM. Figure 7 shows the surface topography of the sol−gel films filled with nanoparticles. It is clear that the alloy samples were covered by the sol−gel layers having similar topographic features. However, the nanocomposite sol−gel films appear to have higher roughness than

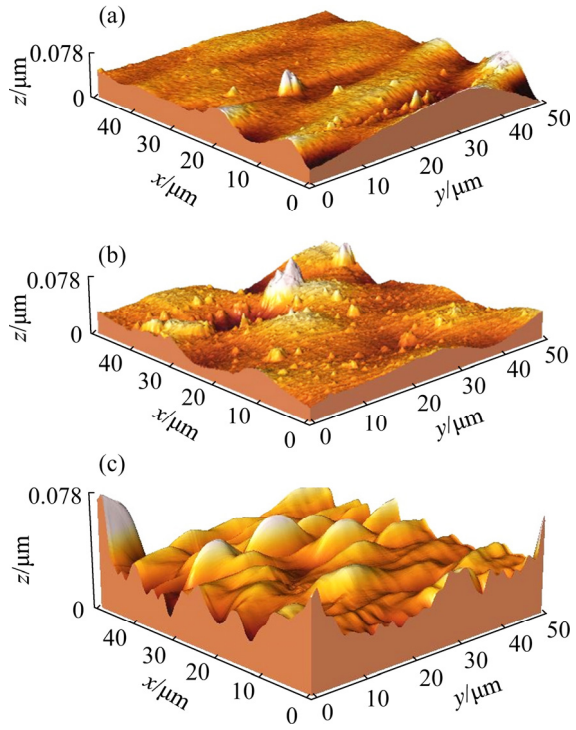

Fig. 7 Topographic AFM images of sol−gel films containing 0 (a), 0.005 (b) and 0.02 wt.% (c) of HND particles

the pure film. The average roughness (R_a) of the pure sol−gel film was about 6.7 nm while the corresponding values after incorporation of 0.005 and 0.02 wt.% of the hydroxylated nanodiamonds were 16.1 and 20.2 nm, respectively. So, the surface roughness was increased by addition of the nanoparticles into the sol−gel film as previously reported for other types of the sol−gel nanocomposites [41−43].

3.3 Corrosion measurements

The influence of the HND particles on the corrosion resistance of the sol−gel coatings was evaluated by the EIS. The impedance responses of the sol−gel coatings (in the form of Nyquist, and phase Bode plots) containing various amounts of the HND nanoparticles after 15, 30, 60 and 120 min immersion in Harrison's corrosive solution are shown in Figs. 8, 9, 10 and 11, respectively. The EIS response of the sol−gel coating containing 0.01 wt.% of the raw ND particles was also obtained to reveal the effect of the hydroxylation process (Fig. 12).

Zero frequency limit of the impedance module ($|Z|_{f\to 0}$) can be regarded as a measure of the corrosion resistance. A significant increment in $|Z|_{f\to 0}$ of the nanocomposites containing hydroxylated nanoparticles was observed with respect to the neat coating over the immersion period and the best results were observed when 0.01 wt.% of the HND particles was used.

The Nyquist plots of the neat and nanocomposite coatings showed three capacitive semicircles at high, medium and low frequency ranges plus an inductive semicircle at the lowest frequencies. The first semicircle on the left side of the Nyquist plots can be ascribed to the outer sol−gel layer. The second arc is attributed to the nanometric inner layer as product of the chemical reaction between the alloy surface and initial sol solution which has been previously discussed in literatures [40,44]. Also, the last capacitive semicircle is related to the natural oxide/hydroxide film on the magnesium alloy. In addition, the

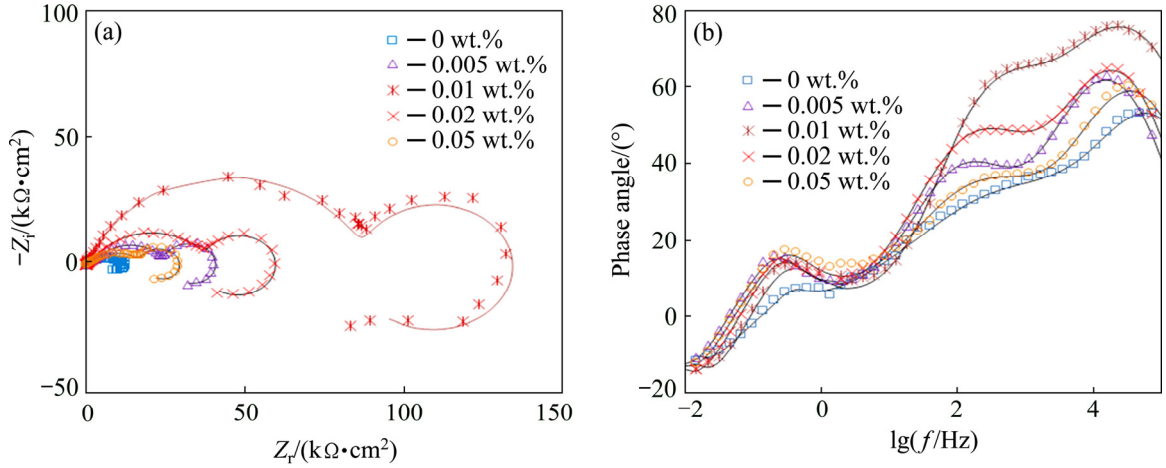

Fig. 8 Impedance response of nanocomposite films with different concentrations of HND particles after 15 min exposure in Harrison's solution: (a) Nyquist plots; (b) Bode plots

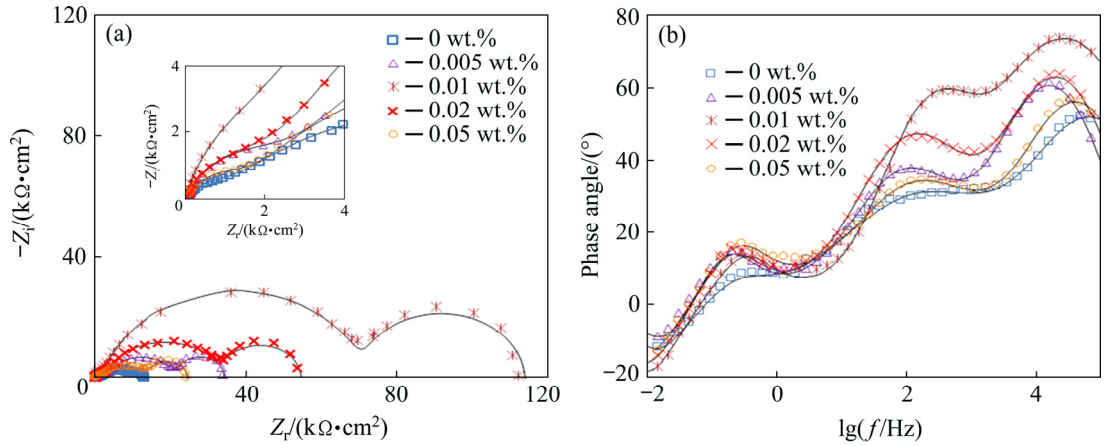

Fig. 9 Impedance response of nanocomposite films with different concentrations of HND particles after 30 min exposure in Harrison's solution: (a) Nyquist plots; (b) Bode plots

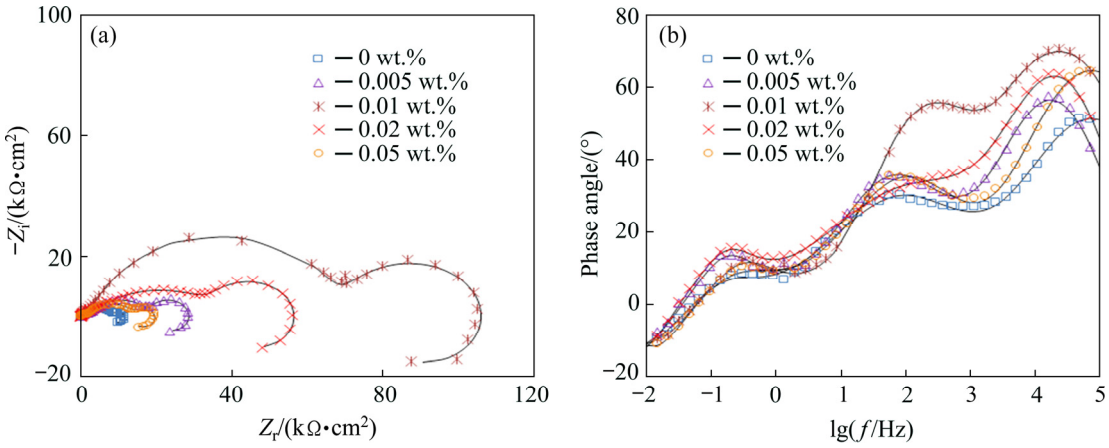

Fig. 10 Impedance response of nanocomposite films with different concentrations of HND particles after 60 min exposure in Harrison's solution: (a) Nyquist plots; (b) Bode plots

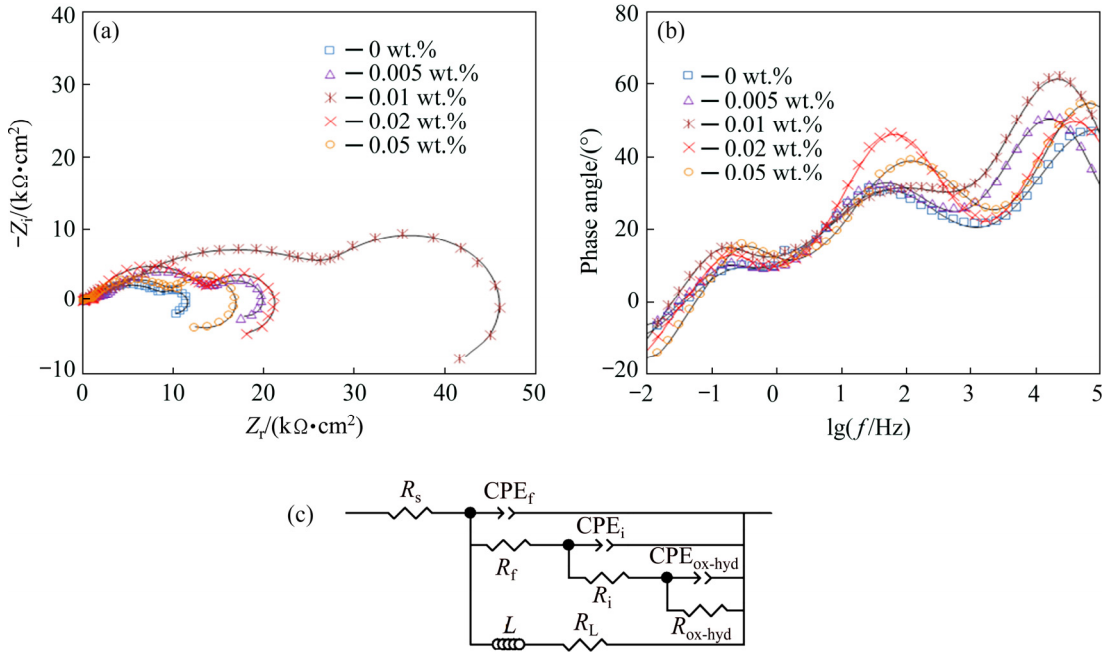

Fig. 11 Impedance response of nanocomposite films with different concentrations of HND particles after 120 min exposure in Harrison's solution: (a) Nyquist plots; (b) Bode plots; (c) Suitable equivalent circuit

inductive arc in the Nyquist plots is typically observed for the magnesium alloy in the aqueous corrosive solution [40]. A suitable circuit model having three capacitive and one inductive time constants was used to fit the experimental EIS data (Fig. 11(c)). In this circuit, R_s, R_f, R_i and $R_{ox\text{-}hyd}$ describe the resistive behaviour of the corrosive electrolyte, outer sol−gel film, inner layer and oxide/hydroxide layer, respectively. Moreover, three constant phase elements (CPE), including CPE_f, CPE_i and $CPE_{ox\text{-}hyd}$, were used to account for the non-ideal capacitive behaviour of the sol−gel film, the inner layer and the oxide/hydroxide layer, respectively. The fitting curves were superimposed on the experimental plots and the extracted quantitative results were plotted versus the immersion time in Fig. 13. The polarization resistance (R_p) values were calculated as $R_p=R_f+R_i+R_{ox\text{-}hyd}$. Also, Q_f, Q_i and $Q_{ox\text{-}hyd}$ are the constants of the CPE_f, CPE_i, and $CPE_{ox\text{-}hyd}$ elements, respectively (Fig. 13). By comparison of the EIS results of the pure sol−gel coating with those previously reported for the bare AM60B alloy [40], significant improvement in the corrosion resistance was revealed. The polarization resistance of the pure sol−gel coating was mildly increased by

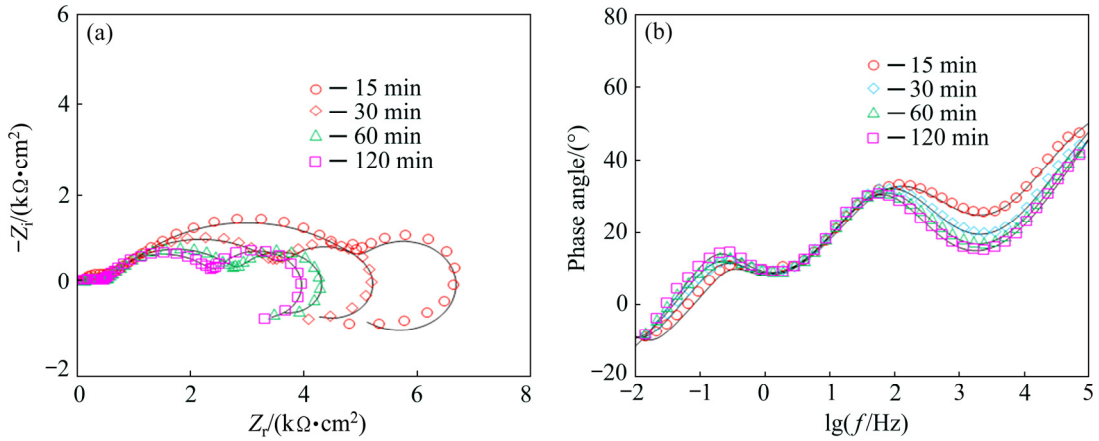

Fig. 12 Impedance response of nanocomposite films containing 0.01 wt.% of unhydrolyzed ND particles after various immersion time in Harrison's solution: (a) Nyquist plots; (b) Bode plots

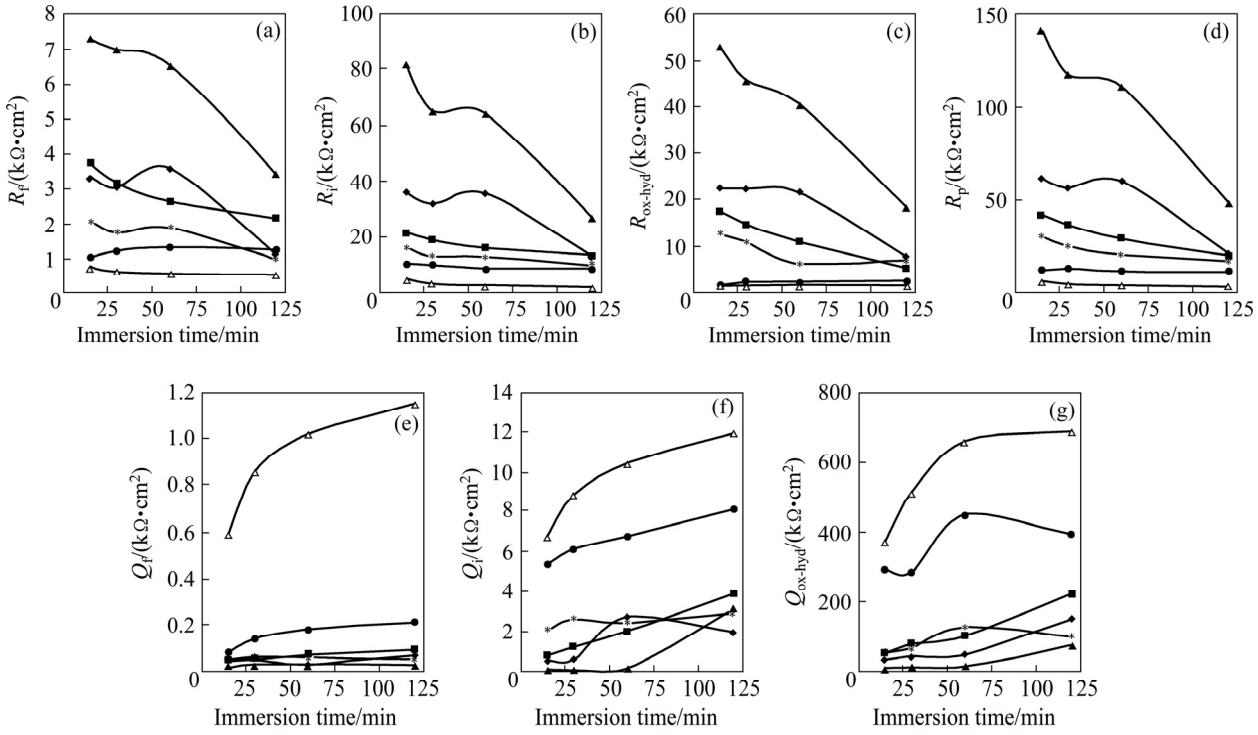

Fig. 13 Changes of extracted impedance parameters versus immersion time in corrosive solution

extending the immersion time from 15 to 30 min more probably due to the filling of the micrometric defects (Figs. 4(a, b)) with the corrosion products. However, the polarization resistance of the mentioned sample was gradually decreased by increasing the exposure time due to the penetration of the corrosive solution toward the alloy surface.

The polarization resistance of the pure sol−gel coating was remarkably improved after incorporation of the HND particles over the whole immersion time. The best results were obtained after addition of 0.01 wt.% of the HND particles to the sol−gel coating. For instance, the polarization resistance of the sol−gel coating was increased from 12.09 to 111.01 kΩ·cm^2 after 60 min immersion after incorporating 0.01 wt.% of the HND particles, indicating significant improvement in the corrosion protection. Incorporation of the HND particles into the sol−gel coating increases its network compactness and integrity because of the strong chemical interaction between the HND particle and sol−gel coating (Fig. 5), leading to the better corrosion protection. Incomplete cross-linking due to the incomplete hydrolysis of the precursors as well as the steric hindrances leading to the low compactness is considered as one of the main drawbacks of the sol−gel coatings. It appears that the chemical interaction of the hydroxylated nanoparticles with the silanol molecules in the initial sol solution (via water condensation reaction) leads to an increase in the density of final sol−gel coatings, which results in improved corrosion protection properties [45,46]. Generally, hydrolysis of the metalosiloxan (Mg—O—Si) bonds at the coating/substrate interface and the polysiloxane network due to the penetration of the corrosive solution are responsible for the film detachments and degradation, respectively [47,48]. After the addition of the HND particles, these problems were resolved due to the formation of much denser sol−gel coatings which effectively resist against the penetration of the aqueous corrosive solution. Also, the embedded HND particles force the corrosive electrolyte to penetrate from longer tortuous pathways in the coatings. In addition, the HND particles fill the structural defects in the sol−gel coating, which leads to the better corrosion protection. However, when the HND content was increased from 0.01 to 0.02 and 0.05 wt.%, its beneficial influence on the R_p was gradually decreased at all the immersion time, maybe due to the partial agglomeration (Fig. 13).

The R_p value of the coating containing different contents of the HND particles were generally decreased by extending the immersion time due to gradual penetration of the corrosive solution through the micro and nano-metric defects. However, the polarization resistance of the sol−gel nanocomposite containing 0.01 wt.% of the HND particles was at least 4 times higher than that observed for the neat sol−gel coating as indication of its better protection capacity against the corrosion (Fig. 13).

As indicator of the sol−gel film capacitance, the values of the Q_f for all of the applied coatings were generally increased by increasing the exposure time certainly due to the diffusion of the aqueous electrolyte into the sol−gel coating (Fig. 13). The lowest Q_f values over the whole exposure period were seen for the sol−gel nanocomposite containing 0.01 wt.% of the HND particles indicating its more compact structure which limits the amounts of the diffused electrolyte leading to the better corrosion protection. Exceptionally, the Q_f values for the sol−gel coating containing 0.02 wt.% of the HNDs were mildly decreased by extending the immersion time from 30 to 60 min. This unusual behaviour may be related to the coating blistering due to the accumulation of the hydrogen gas bubbles as result of undercoating corrosion. The same behaviour was shown for the sol−gel nanocomposite containing the highest concentration of the HND particles by extending the immersion time from 60 to 120 min.

The sol−gel coating containing 0.01 wt.% of the unhydrolysed ND particles has lower polarization resistance not only than the corresponding HND containing coating but also than the pure sol−gel coating (Fig. 13). This result is more probably related to the agglomeration of the ND particles due to their weak chemical interaction with the silane network, as shown in Fig. 5.

The potentiodynamic polarization tests were also performed in the same corrosive media as complementary of the EIS experiments (Fig. 14).

The recorded polarization curves were analyzed using the cathodic Tafel extrapolation technique [49] and the results including corrosion potential (φ_{corr}), cathodic Tafel slope (b_c), and corrosion current density (J_{corr}) were collected in Table 1. The J_{corr} of the neat sol−gel coating was

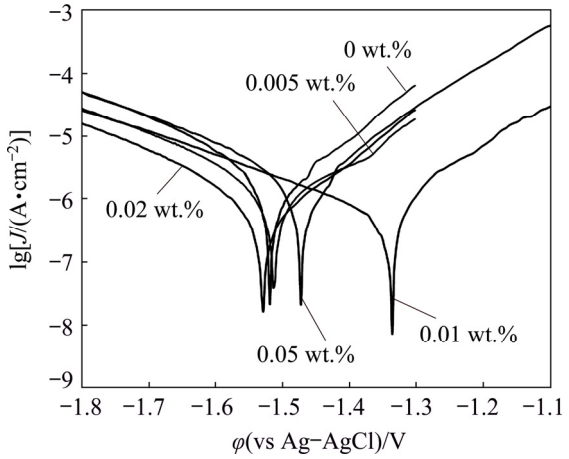

Fig. 14 Potentiodynamic polarization curves of coated samples after 3 h immersion in Harrison's solution

decreased by the addition of the HND nanoparticles in 0.005 wt.% concentration. This effect was promoted by increasing the HND content of the coating to 0.01 wt.% so that the lowest J_{corr} was obtained among the tested samples. However, the corrosion current density of the coated sample was mildly increased by further increasing of the HND content to 0.02 and 0.05 wt.%. However, all of the nanocomposites showed lower corrosion current density than the neat sol−gel coating. These results are in consistent with those obtained by the EIS method.

Table 1 Polarization parameters obtained for nanocomposite sol−gel coatings after 3 h immersion in Harrison's solution

HND content/wt.%	φ_{corr} (vs Ag−AgCl)/V	b_c/ (mV·dec^{-1})	J_{corr}/ (μA·cm^{-2})
0	−1.519	182	2.202
0.005	−1.511	193	1.305
0.01	−1.335	264	0.476
0.02	−1.527	189	0.745
0.05	−1.473	214	1.884

Surface morphologies of the sol−gel coatings containing different contents of the HND particles after the corrosion tests were studied by the SEM in order to confirm the results of the EIS studies (Fig. 15). The SEM images of the coatings with 0

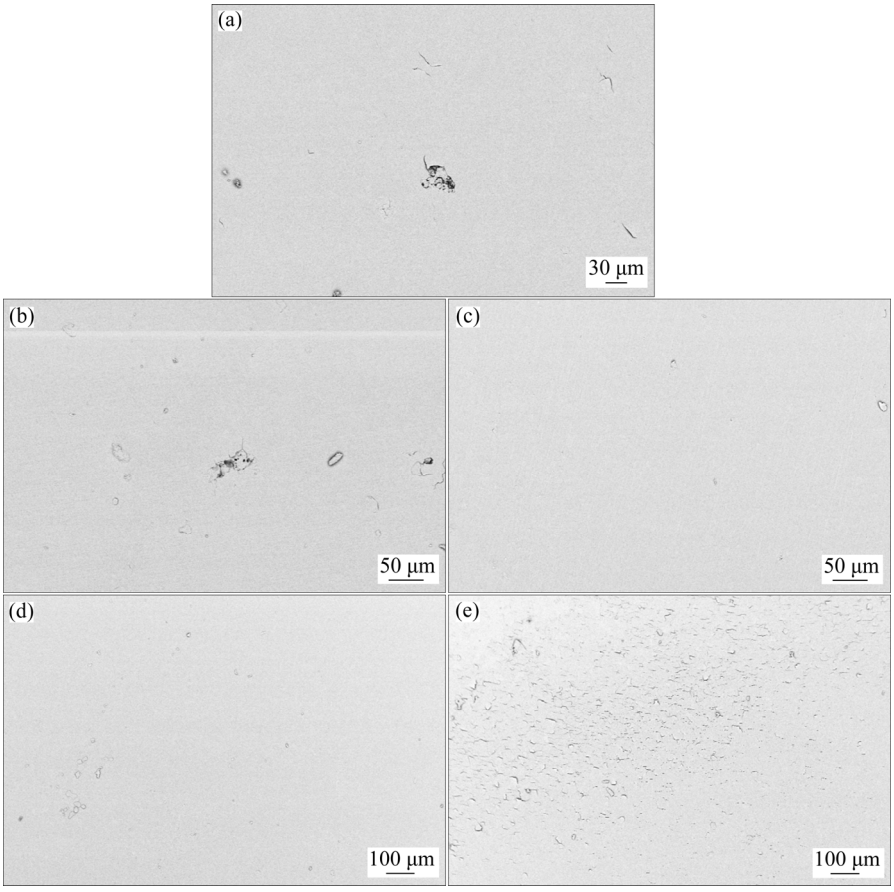

Fig. 15 SEM images of silane coating containing 0 (a), 0.005 (b), 0.01 (c), 0.02 (d) and 0.05 wt.% (e) of HND particles after corrosion tests

and 0.005 wt.% nanoparticles show localized corrosion signs while no visible signs of the corrosion and film delamination are shown in the case of the sol−gel films filled with 0.01 and 0.02 wt.% HND particles, demonstrating their suitable corrosion protection capacity. But, the sol−gel layer delamination can be clearly observed for the coating containing 0.05 wt.% of the HND particles due to the penetration of the corrosive electrolyte in the substrate/coating interfacial region leading to the breakage of the Mg—O—Si bonds. This finding is in good agreement with that obtained by the EIS measurements.

4 Conclusions

(1) The sol−gel coatings containing various concentrations (0−0.05 wt.%) of the HNDs were applied on AM60B magnesium alloy. The size and number of the micrometric defects were decreased after incorporating 0.005 wt.% of the HNDs. Also, the micrometric defects completely disappeared by increasing the HND concentration to 0.01−0.05 wt.%.

(2) The average roughness of the sol−gel film was increased after incorporation of the HNDs.

(3) The corrosion resistance of the sol−gel coating was significantly improved by incorporating different contents of the HNDs and the best results were seen for 0.01 wt.%. However, the positive effect on the corrosion resistance gradually disappeared when the nanoparticle content was increased from 0.01 to 0.05 wt.%.

(4) The results obtained by the EIS examination were confirmed by the potentio-dynamic polarization tests.

(5) The SEM images of the sol−gel coatings with 0 and 0.005 wt.% HNDs showed localized corrosion signs after the corrosion tests while no visible evidence of the corrosion and film delamination were observed for the sol−gel films filled with 0.01 and 0.02 wt.% of the HNDs.

References

[1] RAJABALIZADEH Z, SEIFZADEH D, HABIBI-YANGJEH A, MESRI GUNDOSHMIAN T, NEZAMDOUST S. Electrochemical noise analysis to examine the corrosion behavior of Ni−P deposit on AM60B alloy plated by Zr pretreatment [J]. Surface and Coatings Technology, 2018, 346: 29−39.

[2] WANG X, LI L, XIE Z H, YU G. Duplex coating combining layered double hydroxide and 8-quinolinol layers on Mg alloy for corrosion protection [J]. Electrochimica Acta, 2018, 283: 1845−1857.

[3] LIU Ai-hui, XU Ji-lin. Preparation and corrosion resistance of superhydrophobic coatings on AZ31 magnesium alloy [J]. Transactions of Nonferrous Metals Society of China, 2018: 28: 2287−2293.

[4] SHOGHI P, SEIFZADEH D, GHOLIZADEH-GHESHLAGHI M, HABIBI-YANGJEH A. Pretreatment-free Ni−P plating on magnesium alloy at low temperatures [J]. Transactions of Nonferrous Metals Society of China, 2018, 28: 2478−2488.

[5] NEZAMDOUST S, SEIFZADEH D. Application of Ce−V/sol−gel composite coating for corrosion protection of AM60B magnesium alloy [J]. Transactions of Nonferrous Metals Society of China, 2017, 27: 352−362.

[6] NAZEER A A, Al-HETLANI E, AMIN M O, QUINONES-RUIZ T, LEDNEV I K. A poly(butyl methacrylate)/graphene oxide/TiO_2 nanocomposite coating with superior corrosion protection for AZ31 alloy in chloride solution [J]. Chemical Engineering Journal, 2019, 361: 485−498.

[7] RAJABALIZADEH Z, SEIFZADEH D. Application of electroless Ni−P coating on magnesium alloy via CrO_3/HF free titanate pretreatment [J]. Applied Surface Science, 2017, 422: 696−709.

[8] SAJI V S. Organic conversion coatings for magnesium and its alloys [J]. Journal of Industrial and Engineering Chemistry, 2019, 75: 20−37.

[9] LI D, CHEN F, XIE Z H, SHAN S, ZHONG C J. Enhancing structure integrity and corrosion resistance of Mg alloy by a two-step deposition to avoid F ions etching to nano-SiO_2 reinforcement [J]. Journal of Alloys Compounds, 2017, 705: 70−78.

[10] PEZZATO L, ANGELINI V, BRUNELLI K, MARTINI C, DABALA M. Tribological and corrosion behavior of PEO coatings with graphite nanoparticles on AZ91 and AZ80 magnesium alloys [J]. Transactions of Nonferrous Metals Society of China, 2018, 28: 259−272.

[11] ZHOU H M, CHEN R R, LIU Q, LIU J Y, YU J, WANG C, ZHANG M L, LIU P L, WANG J. Fabrication of ZnO/epoxy resin superhydrophobic coating on AZ31 magnesium alloy [J]. Chemical Engineering Journal, 2019, 368: 261−272.

[12] ZHANG J, XIE Z H, CHEN H, HU C, LI L X, HU B N, SONG Z W, YAN D L, YU G. Electroless deposition and characterization of a double-layered Ni−B/Ni−P coating on AZ91D Mg alloy from eco-friendly fluoride-free baths [J]. Surface and Coatings Technology, 2018, 342: 178−189.

[13] CHEN S, ZHAO S, CHEN M Y, ZHANG X, ZHANG J, LI X, ZHANG H, SHEN X L, WANG J, HUANG N. The anticorrosion mechanism of phenolic conversion coating applied on magnesium implants [J]. Applied Surface Science, 2019, 463: 953−967.

[14] ASHASSI-SORKHABI H, MORADI-ALAVIAN S, JAFARI R, KAZEMPOUR A, ASGHARI E. Effect of amino acids and montmorillonite nanoparticles on improving the corrosion protection characteristics of hybrid sol−gel coating applied on AZ91 Mg alloy [J]. Materials Chemistry and Physics, 2019, 225: 298−308.

[15] DIKICI B, NIINOMI M, TOPUZ M, SAY Y, AKSAKAL B, YILMAZER H, NAKAI M. Synthesis and characterization of hydroxyapatite/TiO_2 coatings on the β-type titanium alloys with different sintering parameters using sol−gel method [J]. Protection of Metals and Physical Chemistry of Surfaces, 2018, 54: 457−462.

[16] ASHRAFI-SHAHRI S M, RAVARI F, SEIFZADEH D. Smart organic/inorganic sol−gel nanocomposite containing functionalized mesoporous silica for corrosion protection [J]. Progress in Organic Coatings, 2019, 133: 44−54.

[17] LI Y, GUAN Y, ZHANG Z, YNAG S. Enhanced bond strength for micro-arc oxidation coating on magnesium alloy via laser surface microstructuring [J]. Applied Surface Science, 2019, 478: 866−871.

[18] WANG D, BIERWAGEN G P. Sol−gel coatings on metals for corrosion protection [J]. Progress in Organic Coatings, 2009, 64: 327−338.

[19] DALMORO V, AZAMBUJA D S, ALEMAN C, ARMELIN E. Hybrid organophosphonic-silane coating for corrosion protection of magnesium alloy AZ91: The influence of acid and alkali pre-treatments [J]. Surface and Coatings Technology, 2019, 357: 728−739.

[20] SUEGAMA P H, RECCO A A C, TSCHIPTSCHIN A P, AOKI I V. Influence of silica nanoparticles added to an organosilane film on carbon steel electrochemical and tribological behavior [J]. Progress in Organic Coatings, 2007, 60: 90−98.

[21] PERES R N, CARDOSO E S F, MONTEMOR M F, de MELO H G, BENEDETTI A V, SUEGAMA P H. Influence of the addition of SiO_2 nanoparticles to a hybrid coating applied on an AZ31 alloy for early corrosion protection [J]. Surface and Coatings Technology, 2016, 303: 372−384.

[22] CLAIRE L, MARIE G, JULIEN G, JEAN-MICHEL S, JEAN R, MARIE-JOELLE M, STEFANO R, MICHELE F. New architectured hybrid sol−gel coatings for wear and corrosion protection of low-carbon steel [J]. Progress in Organic Coatings, 2016, 99: 337−345.

[23] OLIVIER M G, FEDEL M, SCIAMANNA V, VANDERMIERS C, MOTTE C, POELMAN M, DEFLORIAN F. Study of the effect of nanoclay incorporation on the rheological properties and corrosion protection by a silane layer [J]. Progress in Organic Coatings, 2011, 72: 15−20.

[24] ASADI N, NADERI R, SAREMI M. Determination of optimum concentration of cloisite in an eco-friendly silane sol−gel film to improve corrosion resistance of mild steel [J]. Applied Clay Science, 2014, 95: 243−251.

[25] FEDEL M, POELMAN M, ZAGO M, VANDERMIERS C, COSSEMENT D, OLIVIER M G, DEFLORIAN F. Influence of formulation and application parameters on the performances of a sol−gel/clay nanocomposite on the corrosion resistance of hot-dip galvanized steel. Part II. Effect of curing temperature and time [J]. Surface and Coatings Technology, 2015, 274: 9−17.

[26] YU Q, MA X, WANG M, YU C, BAI T. Influence of embedded particles on microstructure, corrosion resistance and thermal conductivity of CuO/SiO_2 and NiO/SiO_2 nanocomposite coatings [J]. Applied Surface Science, 2008, 254: 5089−5094.

[27] CHENG L H, LIU C L, HAN D J, YANG L, GUO W H, CAI H F, WANG X H. Effect of graphene on corrosion resistance of waterborne inorganic zinc-rich coatings [J]. Journal of Alloys and Compounds, 2019, 774: 255−264.

[28] YU M, DONG H, SHI H B, XIONG L L, HE C, LIU J H, LI S M. Effects of graphene oxide-filled sol−gel sealing on the corrosion resistance and paint adhesion of anodized aluminum [J]. Applied Surface Science, 2019, 479: 105−113.

[29] LI J, CUI J C, YANG J Y, MA Y, QIU H, YANG J H. Silanized graphene oxide reinforced organofunctional silane composite coatings for corrosion protection [J]. Progress in Organic Coatings, 2016, 99: 443−451.

[30] RAMEZANZADEH B, AHMADI A, MAHDAVIAN M. Enhancement of the corrosion protection performance and cathodic delamination resistance of epoxy coating through treatment of steel substrate by a novel nanometric sol−gel based silane composite film filled with functionalized graphene oxide nanosheets [J]. Corrosion Science, 2016, 109: 182−205.

[31] LIU Y, CAO H J, YU Y, CHEN S. Corrosion protection of silane coatings modified by carbon nanotubes on stainless steel [J]. Journal of Electrochemical Society, 2015, 10: 3497−3509.

[32] SHEN Bin, CHEN Su-lin, SUN Fang-hong. Effect of deposition temperature on properties of boron-doped diamond films on tungsten carbide substrate [J]. Transactions of Nonferrous Metals Society of China, 2018, 28: 729−738.

[33] AGHAMOHAMMADI H, HEIDARPOUR A, JAMSHIDI R, BAYAT O. Tribological behavior of epoxy composites filled with nanodiamond and Ti3AlC2TiC particles: A comparative study [J]. Ceramics International, 2019, 45: 9106−9113.

[34] CHEN X Y, ZHANG B T, GONG Y F, ZHOU P, LI H. Mechanical properties of nanodiamond-reinforced hydroxyapatite composite coatings deposited by suspension plasma spraying [J]. Applied Surface Science, 2018, 439: 60−65.

[35] KRUGER A, LIANG Y, JARRE G, STEGK J. Surface functionalisation of detonation diamond suitable for biological applications [J]. Journal of Materials Chemistry, 2006, 16: 2322−2328.

[36] KRUEGER A, OZAWA M, JARRE G, LIANG Y, STEGK J, LU L. Deagglomeration and functionalisation of detonation diamond [J]. Physica Status Solidi A, 2007, 204: 2881−2887.

[37] SHENDEROVA O, PANICH A M, MOSEENKOV S, HENS S C, KUZNETSOV V, VIETH H M. Hydroxylated detonation nanodiamond: FTIR, XPS, and NMR studies [J]. Journal of Physical Chemistry C, 2011, 115: 19005−19011.

[38] ZHENG Wen-Wei, HSIEH Yi-Han, CHIU Yu-Chung, CAI Sian-Jhu, CHENG Chia-Liang, CHEN Chinpiao. Organic functionalization of ultradispersed nanodiamond: synthesis and applications [J]. Journal of Materials Chemistry, 2009, 19: 8432−8441.

[39] SHAMES A I, MOGILYANSKY D, PANICH A M, SERGEEV N A, OLSZEWSKI M, BOUDOU J P, OSIPOV V Y. XRD, NMR, and EPR study of polycrystalline micro- and nano-diamonds prepared by a shockwave compression method [J]. Physica Status Solidi A, 2015, 212: 2400−2409.

[40] NEZAMDOUST S, SEIFZADEH D, RAJABALIZADEH Z.

PTMS/OH-MWCNT sol−gel nanocomposite for corrosion protection of magnesium alloy [J]. Surface and Coatings Technology, 2018, 335: 228−240.

[41] LAKSHMI R V, BHARATHIDASAN T, BASU B J. Superhydrophobic sol−gel nanocomposite coatings with enhanced hardness [J]. Applied Surface Science, 2011, 257: 10421−10426.

[42] LAKSHMI R V, BHARATHIDASAN T, BERA P, BASU B J. Fabrication of superhydrophobic and oleophobic sol−gel nanocomposite coating [J]. Surface and Coatings Technology, 2012, 206: 3888−3894.

[43] SUEGAMA P H, RECCO A A, TSCHIPTSCHIN A P, AOKI I V. Influence of silica nanoparticles added to an organosilane film on carbon steel electrochemical and tribological behavior [J]. Progress in Organic Coatings, 2007, 60: 90−98.

[44] WANG H, AKID R, GOBARA M. Scratch-resistant anticorrosion sol−gel coating for the protection of AZ31 magnesium alloy via a low temperature sol−gel route [J]. Corrosion Science, 2010, 52: 2565−2570.

[45] BUTLER TM, MacCRAITH BD, McDONAGH C. Leaching in sol−gel derived silica films for optical pH sensing [J]. Journal of Non-Crystalline Solids, 1998, 224: 249−258.

[46] AKHTAR S, MATIN A, KUMAR A M, IBRAHIM A, LAOUI T. Enhancement of anticorrosion property of 304 stainless steel using silane coatings [J]. Applied Surface Science, 2018, 440: 1286−1297.

[47] QIAN Zhi-qiang. Corrosion behavior study of AZ31B magnesium alloy by sol−gel silica-based hybrid coating [J]. International Journal of Electrochemical Science, 2017, 12: 8269−8279.

[48] JUAN-DIAZ M J, MARTINEZ-IBANEZ M, HERNANDEZ-ESCOLANO M, CABEDO L, IZQUIERDO R, SUAY J, GURRUCHAGA M, GONI I. Study of the degradation of hybrid sol−gel coatings in aqueous medium [J]. Progress in Organic Coatings, 2014, 77: 1799−1806.

[49] CURIONI M, SCENINI F, MONETTA T, BELLUCCI F. Correlation between electrochemical impedance measurements and corrosion rate of magnesium investigated by realtime hydrogen measurement and optical imaging [J]. Electrochimica Acta, 2015, 166: 372−384.

镁合金表面含纳米金刚石的溶胶凝胶耐腐蚀涂层

S. NEZAMDOUST, D. SEIFZADEH, A. HABIBI-YANGJEH

Applied Chemistry Department, Faculty of Science, University of Mohaghegh Ardabili, Ardabili, Iran

摘　要：在镁合金表面涂覆含不同比例羟基化纳米金刚石(HND)颗粒的溶胶凝胶防腐蚀涂层。加入 0.01%、0.02%和 0.05%(质量分数)HND 颗粒后溶胶凝胶涂层中的微缺陷完全消失。AFM 分析表明，加入 0.005%和 0.02%的 HND 颗粒后，溶胶凝胶层的平均粗糙度从约 6.7 nm 分别增加到 16.1 nm 和 20.2 nm。在 Harrison 溶液中分别浸泡 15、30、60 和 120 min 后，用电化学阻抗谱(EIS)技术测试涂层的耐蚀性。加入不同浓度的 HND 颗粒可显著提高溶胶凝胶涂层的耐蚀性，并在 0.01%时获得最佳结果。通过动电位极化试验验证电化学阻抗谱实验的结果。耐腐蚀性的增强是由于涂层的致密性(由于基体与 HND 颗粒产生化学作用)、腐蚀溶液曲折扩散路径的形成以及纳米颗粒对缺陷的填充。然而，随着纳米颗粒含量的增加，HND 对耐腐蚀性的有利影响逐渐减弱。最后，对腐蚀实验后的溶胶凝胶纳米复合涂层的显微形貌进行研究。

关键词：镁合金；腐蚀；涂层；溶胶凝胶；纳米金刚石

(Edited by Bing YANG)